New Journal of Physics
The open-access journal for physics

Vortex matter in oblate mesoscopic superconductors with a hole: broken symmetry vortex states and multi-vortex entry

Ben Xu[1], **M V Milošević**[1,2] **and F M Peeters**[1,3]

[1] Departement Fysica, Universiteit Antwerpen, Groenenborgerlaan 171, B-2020 Antwerpen, Belgium
[2] Department of Physics, University of Bath, Claverton Down, BA2 7AY Bath, UK
E-mail: francois.peeters@ua.ac.be

New Journal of Physics **11** (2009) 013020 (21pp)
Received 19 August 2008
Published 16 January 2009
Online at http://www.njp.org/
doi:10.1088/1367-2630/11/1/013020

Abstract. Using three-dimensional (3D) numerical discretization of the Ginzburg–Landau (GL) equations, we investigate the superconducting state of a sphere with a piercing hole in the presence of a magnetic field. In the case of samples with central perforation, in axially applied homogeneous magnetic field, we realized unconventional vortex states of broken symmetry due to complex, 3D competing interactions, which depend on the GL parameter κ. For certain sizes of the sample, non-hysteretic multi-vortex entry and exit is predicted with the non-existence of some vorticities as stable states. In a tilted magnetic field, we studied the gradual transformation of 3D flux patterns into 1D vortex chains, where vortices align along the perforation, and the evolvement of the multi-vortex entry as well. We analyze the flux-guiding ability of the hole in a tilted field, which leads to fractional flux response in magnetization $M(H)$ curves.

[3] Author to whom any correspondence should be addressed.

Contents

1. Introduction

During the past decade, the properties of mesoscopic superconductors became one of the major directions in the research in superconductivity. In thin, practically two-dimensional (2D) samples, the superconducting state is strongly influenced by the sample geometry in the plane. So-called vortex matter deals with flux patterns in superconductors in applied magnetic field, and becomes particularly rich in truly 3D samples, as both geometry and the orientation of the magnetic field must be taken into account. Applications of superconductors in electronic circuits and ultra-high field magnets require knowledge and control of the behavior of critical parameters of the sample, i.e. critical temperature T_c, critical current J_c and critical magnetic field H_c [1]. The latter is of particular interest in mesoscopic superconductors, which easily exhibit an increase of the critical field beyond H_{c2}, the characteristic magnetic field value for type-II superconductors. Further enhancement of H_c is feasible by introducing perforations in the sample, which trap the applied field and reduce the effective field in the superconducting material. Such a study was done by Baelus *et al* [2] for a thin superconducting disk with a hole. The hole provides a trap for the magnetic flux, and helps to establish the paramagnetic response of the sample. The number of trapped magnetic flux quanta depends on the size of the hole, which determines the final arrangement of vortices into a giant- or multi-vortex state (a multi-quanta vortex versus a collection of individual vortices on a shell) in the superconductor. The same work also reports the symmetry-breaking of the vortex state by shifting the hole away from sample's center leading to 1D-like vortices [3], which were recently observed [4].

Furthermore, introduction of holes in superconducting samples leads to an increase of J_c as well, since perforations limit the mobility of the flux lines (and are therefore called vortex pinning centers) which in turn prevents dissipation [5]. In this respect, most theoretical and experimental works up to now were restricted to 2D samples, i.e. patterned films and thin polygons [6]–[8]. Tunable pinning can be achieved by changing the 3D geometry of the pinning centers, such as in the case of blind holes where thickness of the bottom layer determines the pinning strength [9]. Recently, advances in sample fabrication, nano-lithography and electrochemistry, made possible experiments on 3D samples of controlled geometry [10]. Therefore, it is timely to bring forward the corresponding theoretical analysis, and several very recent works have set grounds for understanding of vortex matter in 3D. For example, spherical superconducting shells were studied by Du [11] and recently revisited by Gladilin *et al* [12], with the restriction of extremely small thickness. Nucleation of superconductivity in type-II spherical superconductors was calculated in [13] and the extension to different boundary

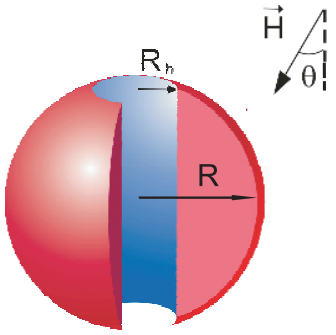

Figure 1. The oblique view of the spherical sample (radius R) with a cylindrical perforation of radius R_h in applied magnetic field H under a tilt angle θ.

conditions in [14]. Extreme type-II superconducting cylinders were studied in a tilted magnetic field in [15], and [16] reports a study of vortex matter with full consideration of demagnetization effects, for the case of mesoscopic spheres.

The role of pinning centers in 3D was only studied for the case of bulk samples. Doria and Zebende [17] investigated superconductors with a cubic array of pinning centers with a size comparable to the coherence length. They established the conditions for entrance of vortices into the pinning center, and studied the maximal possible number of vortices that fit inside. Pinned vortex lines exhibited a clear 3D nature, often interacting towards a triangular vortex lattice away from the pinning centers, while curving towards a square arrangement in the vicinity of the pinning sites.

In this paper, we analyze the influence of confinement on flux trapping by a hole or cavity, due to the presence of the sample boundary (unlike the bulk case). For comparison with earlier works, we preserve the oblate shape of the sample, and study the influence of complete or partial perforation on vortex matter, and that for the case of radially symmetric and non-symmetric samples. In addition, we investigate vortex structure transitions in a tilted magnetic field.

This paper is organized as follows. The studied samples and theoretical formulation of the problem are presented in section 2. The vortex states in spherical samples with a centered cylindrical perforation in axial magnetic field are discussed in section 3. We introduce 3D asymmetry to the system, by tilting the magnetic field acting on the samples in section 4. The conclusions are presented in section 5.

2. Theoretical approach

We consider type II superconducting samples (i.e. for characteristic lengths $\lambda > \xi$), of spherical shape with radius R with a piercing hole of radius R_h respectively (see figure 1). These samples are immersed in an insulating medium (e.g. air or vacuum), and exposed to a uniform magnetic field H, applied under a tilt angle θ with respect to the z-axis. Using dimensionless variables and the London gauge div $\vec{A} = 0$ for the vector potential $\vec{A}$, we write the system of two coupled Ginzburg-Landau (GL) equations in the following form

$$(-\mathrm{i}\vec{\nabla} - \vec{A})^2\Psi = \Psi(1 - |\Psi|^2), \tag{1}$$

$$-\kappa^2\Delta\vec{A} = \frac{1}{2\mathrm{i}}(\Psi^*\vec{\nabla}\Psi - \Psi\vec{\nabla}\Psi^*) - |\Psi|^2\vec{A}, \tag{2}$$

where the right side of equation (2) is the density of the superconducting current $\vec{j}$ induced by the sample in response to the applied field. Here the distance is measured in units of the coherence length ξ, the vector potential A in $c\hbar/2e\xi^2 = \kappa\sqrt{2}H_c$, and the order parameter Ψ is scaled to its value in the absence of the magnetic field. The GL parameter equals $\kappa = \lambda/\xi$, where ξ and λ are coherence length and penetration depth, respectively. To numerically treat this system, we discretize equations (1) and (2) on a uniform cubic grid using the link variable approach [18, 19], with typically five grid points per ξ, and solve the equations self-consistently in a finite-difference scheme, where equation (2) is solved using 3D fast Fourier transform.

In our calculations, the superconducting order parameter satisfies the Neumann boundary condition on the sample surface, as well as on the boundaries of the hole

$$(-\mathrm{i}\vec{\nabla} - \vec{A})\Psi|_{\rho=R \text{ and } r=R_h} = 0, \tag{3}$$

while the initially applied vector potential A_0 takes the form $A_{0x} = -\frac{1}{2}H(y\cos\theta - z\sin\theta)$, $A_{0y} = \frac{1}{2}Hx\cos\theta$ and $A_{0z} = -\frac{1}{2}Hx\sin\theta$.

The convergent solution of equations (1) and (2) gives a superconducting state as a local energy minimum. In search for all stable states for given conditions (thus the lowest energy *ground* state, and the higher energy *metastable* states), we repeat the calculation using different initial conditions. For a realistic comparison with a field-cooled experiment, we initiate the calculation from randomly generated and very weak superconducting order parameter, while in a zero-field-cooled situation, we start from $\Psi \approx 1$ in the whole sample. Once a solution is found, we are able to trace that state back and forth in its whole field stability range, by gradually sweeping up/down the applied magnetic field and recalculate each time the superconducting state starting from the previously found one. For all found vortex configurations we calculate the Gibbs free energy (in units of $F_0 = H_{c2}^2/8\pi$, where $H_{c2} = c\hbar/2e\xi^2 = \sqrt{2}\kappa H_{c1} = \Phi_0/2\pi\xi^2$), as

$$F = \frac{1}{V}\int_V [2(\vec{A} - \vec{A}_0)\cdot\vec{j} - |\Psi|^4]\mathrm{d}^3r, \tag{4}$$

where integration is performed over the sample volume V. Comparison of obtained energy levels of different vortex states enables us to discuss their (meta-)stability as a function of relevant parameters.

The solution of equation (2) enables us to calculate the magnetic field emerging from the superconductor in response to the applied magnetic field. To characterize this effective expulsion of magnetic flux, we calculate magnetization of the sample in applied field. Instead of the known thermodynamic expression $M = \partial F/\partial H$, we define sample magnetization in accordance with experimental reality, i.e. as the expelled magnetic field from the sample

$$\vec{M} = \frac{\langle\vec{h}\rangle - \vec{H}}{4\pi}, \tag{5}$$

where $\vec{h} = \mathrm{rot}\vec{A}$ is the resulting (total) magnetic field, and $\langle\ \rangle$ denotes averaging over the particular area (which could be the sample as a whole, or just a surface area of a magnetic detector at a given location with respect to the sample).

3. Spherical samples with a perforation, in axial magnetic field

In what follows, we consider the superconducting sphere with a cylindrical perforation, in applied field parallel to the perforation ($\theta = 0^\circ$). Figure 2 shows the free energy of the found

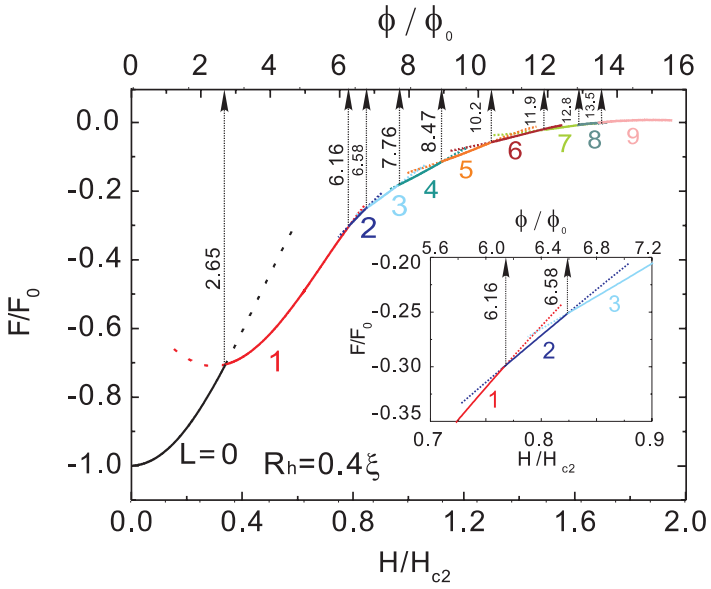

Figure 2. The free energy curves as a function of the applied magnetic field ($\theta = 0^\circ$), in units of $F_0 = H_{c2}^2/4\pi$, for a superconducting sphere with radius $R = 4\xi$, with a centered cylindrical hole of radius $R_h = 0.4\xi$. The upper x-axis gives the applied flux through the equator of the sphere. Metastable states are shown by dotted curves. The inset shows a zoom of the energy levels for states with vorticity $L = 1, 2$ and 3.

vortex states as function of the magnetic field, for a sample of radius $R = 4\xi$, made of strong type-II material (we took $\kappa > 10$ everywhere in the paper, except as otherwise indicated) with a cylinder hole of radius $R_h = 0.4\xi$. The first vortex enters in the ground state for field $H = 0.34H_{c2}$, corresponding to an applied flux through the equatorial plane of $\Phi \approx 2.65\Phi_0$. Such very effective screening of flux is characteristic of mesoscopic superconductors, and has already been observed in superconducting disks [2]. However, in our case the Meissner state is followed by a pronounced stable $L = 1$ state (L being the vorticity), which remains in the ground state over a field range of $\Delta H = 0.42H_{c2}$—corresponding to the additional flux of over $3.47\Phi_0$! Surprisingly, the subsequent vortex states show rather conventional stability ranges corresponding roughly to the addition of a single flux quantum, except the $L = 2$ state which is found in the ground state only for $0.77 < H/H_{c2} < 0.82$, i.e. for $\Delta\Phi \approx 0.42\Phi_0$ (see inset of figure 2). Thus, the $L = 1$ state exhibits pronounced stability at the expense of the $L = 2$ state.

To understand this, we examined closely the vortex configurations themselves, some of which are shown in figure 3 as the Cooper-pair density plots on the surface of the sample. Contrary to the known vortex states found in mesoscopic spheres [16], in the present case there is always a vortex located in the center of the sample, pinned by the hole. It is already well established that maximal number of vortices that can be pinned by a cylindrical hole depends on the hole radius and is usually called the saturation number n_s [20, 21]. For $R_h = 0.4\xi$ we found that n_s equals one, the following, second vortex in the sample cannot reside in the hole, and Bean–Livingston (BL) barrier for its entry is enforced by the repulsion from the already pinned first vortex. Eventually, at significantly higher field, vortex enters the sample but *remains located at the periphery*, resulting in a cylindrically asymmetric degenerate state shown in figure 3(a).

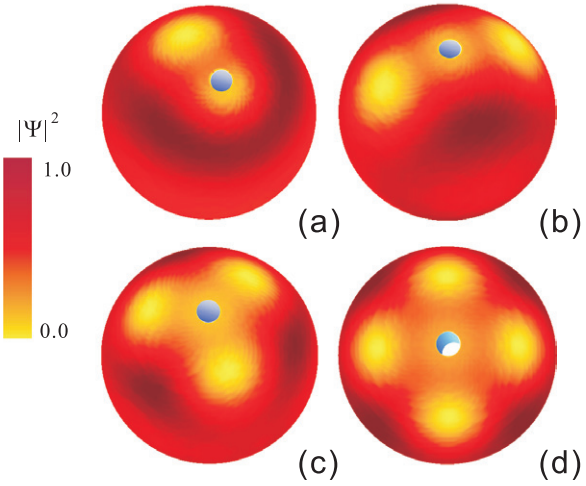

Figure 3. The surface plots of the Cooper-pair density for a $R = 4\xi$ superconducting sphere with a cylindrical hole of radius $R_h = 0.4\xi$. The figures show the $(n_o, L) = (1,2)$ (a), (1,3) (b), (1,4) (c) and (1,5) (d) multi-vortex states (n_o is the hole occupation number, L the vorticity).

This unique state was never predicted before for radially symmetric samples in a homogeneous field, but somewhat similar symmetry breaking (in appearance, not origin) was found in disks with magnetic coating [22].

For clarity, we adopt here the notation (n_o, L) for the vortex state, where n_o gives the actual number of vortices in the hole, i.e. the hole occupation number. Figures 3(b)–(d) show the states $(n_o, L) = (1,3–5)$, respectively, and illustrate ordering of additional vortices on a ring around the central hole (and the pinned vortex).

Obviously, the vortex structure in the considered samples is strongly affected by the size of the hole. Figure 4 shows the free energy plot for a sample with a larger hole of radius $R_h = 1.2\xi$. Compared with figure 2, the critical magnetic field for superconducting-to-normal state transition becomes higher, as larger hole facilitates in general the expulsion of the magnetic field from the superconducting material. Nevertheless, the first vortex penetration field is *two times* lower for the sample with $R_h = 1.2\xi$, as a larger hole also attracts more magnetic flux inside the hole. $L = 1$ vortex state is thus found to be very stable for both samples, but the $L = 2$ state exhibits very different behavior, becoming far more stable for a larger hole radius. The explanation lies in the hole occupation number n_o, which becomes larger with hole radius, and equals 2 for $R_h = 1.2\xi$. In other words, the $L = 2$ state becomes a giant-vortex of vorticity 2 trapped in the hole, which preserves the radial symmetry and has enhanced stability compared to the broken symmetry $L = 2$ state found for $R_h = 0.4\xi$.

Having obtained the complete energy spectra for different vortex configurations for samples with $R = 4\xi$ and the hole radius R_h varying from 0 to 2.2ξ, we were able to construct an equilibrium vortex phase diagram that is shown in figure 5 as a function of the magnetic field H. The Meissner state is found to be less stable with increasing hole radius because the bigger sized hole more easily accommodates a vortex. And the flux trapped inside the hole can be calculated as: $\Phi = BS = n\Phi_0$ and because $S = \pi R_h^2$; therefore we have $B \sim n/R_h^2$. But this is only true if the hole is big enough to accommodate a vortex, i.e. $R_h > \xi$, otherwise

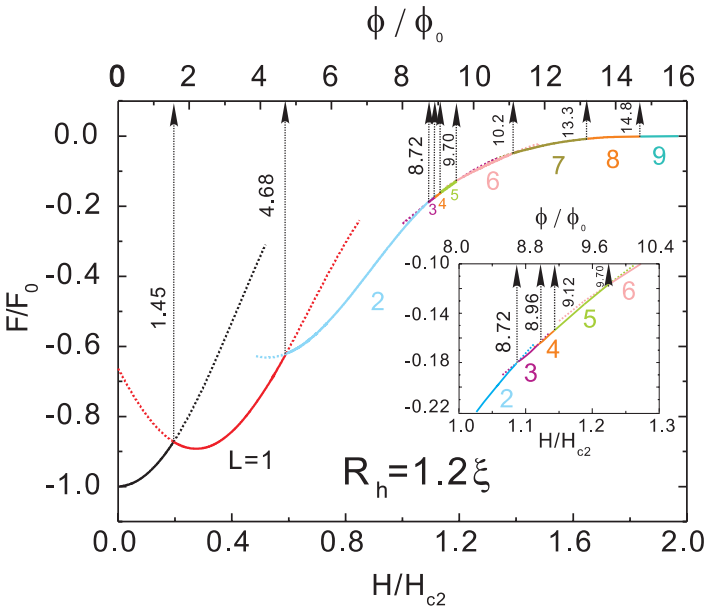

Figure 4. The free energy curves as a function of the applied magnetic field, for $R = 4\xi$ and $R_h = 1.2\xi$. Same notation as in figure 2 is used. The inset shows a zoom of the energy levels for states with vorticity $L = 2, 3, 4, 5$ and 6.

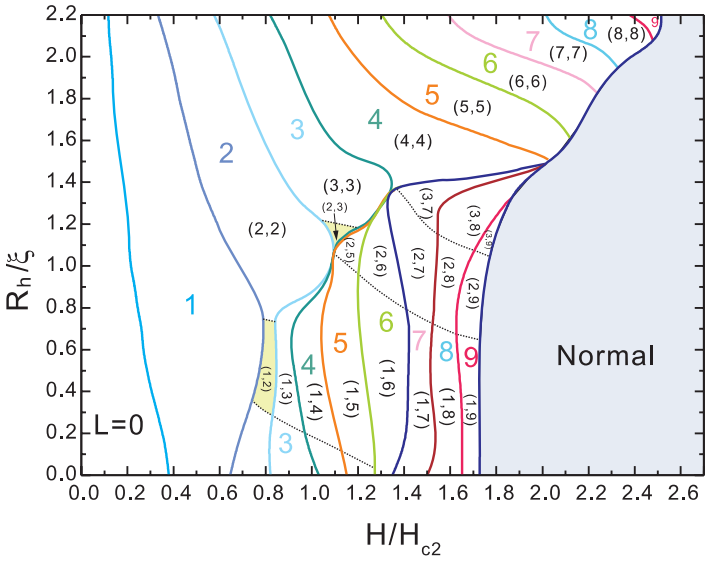

Figure 5. The ground-state vortex phase diagram. Solid lines show the relation between the hole radius R_h and the applied magnetic field H at which the $L \to L+1$ transitions take place for a superconducting sphere of radius $R = 4.0\xi$. Shaded regions denote the parameter values at which broken-symmetry vortex states are stabilized. The regions with different hole-occupation n_o are separated by dashed lines.

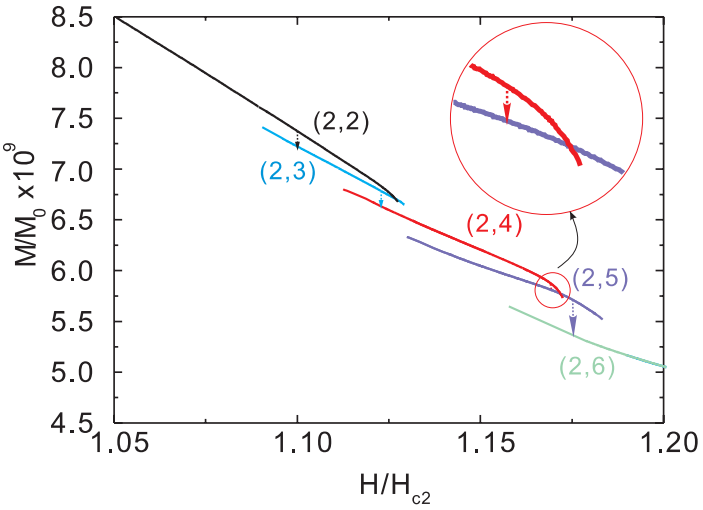

Figure 6. The magnetization curves for vortex states (2,2), (2,3), (2,4) and (2,5), corresponding to the states shown in the inset of figure 4. Solid lines index the stable states for field sweep up/down, while the vertical dotted lines show the equilibrium transition points. Insert magnifies the area where equilibrium transition happens for vortex state changing from (2,4) to (2,5).

only one vortex can be accommodated. The critical field of the sample increase with hole size, especially for sample with $R_h > 1.4\xi$, where the surface superconductivity is greatly enhanced. While the maximal vorticity remains the same (i.e. $L_{max} = 9$), when $R_h < 2.2\xi$. For each vortex state with $n_o < L \leqslant L_{max}$, n_o vortices can be trapped in the hole, all the other $L - n_o$ vortices have to nucleate in the superconducting area to form a shell. And to first-order the magnetic field for nucleation of the next vortex will be almost independent of the hole radius when R_h is smaller or of the order of ξ. Different vortex states exist for a certain vorticity in the same sized SC sample, between which first-order transitions are found when magnetic field changes, like (2,7) and (3,7) for $L = 7$ vortex state. Shaded areas indicate the stability regions of the broken-symmetry states, and are always followed by 'necking' of the transition lines towards adjacent vortex states. In other words, each asymmetric state has a narrower stability region than a corresponding symmetric state. Besides the already discussed $L = 2$ state for smaller holes, an asymmetric vortex state was also found for $L = 3$ states as well, obviously for the hole size allowing for a larger occupation number (in this case $n_o = 2$). Similarly to the $R_h = 0.5\xi$ case, we found very narrow regions of stability for the radially asymmetric vortex states in figure 5—e.g. for $0.95\xi < R_h < 1.2\xi$, note the suppressed $L = 2 \to 3 \to 4 \to 5$ transition with increasing field (see also figure 4). In addition to the disfavored symmetry of the states (asymmetric (2,3), and linear (2,4) state), the competition between the flux expulsion, additional vortices being repelled by the ones already in the hole, and the magnetic pressure inwards, also contributes to this 'necking' effect. As a result of these competing interactions, the transitions between the aforementioned states are weakly first-order. This is clear from the magnetization curves for the $R_h = 1.2\xi$ case shown in figure 6. The magnetization of the sample is weakly discontinuous for the thermodynamic transition from the vortex states (2,2) to (2,3), as well as for the transition between states (2,4) and (2,5). This explains the weak first-order manifestation of those phase transitions but the vortex entry in superconductors is of course always of first-order.

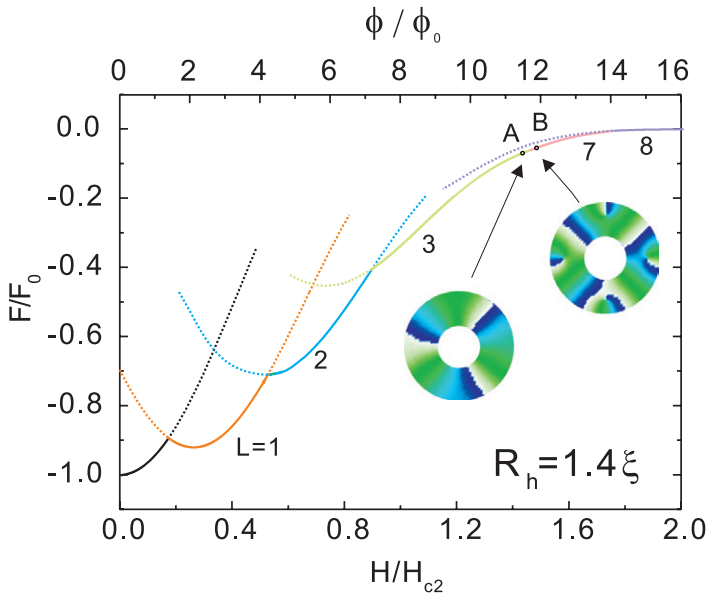

Figure 7. The free energy curves are plotted versus the applied magnetic field, for $R = 4\xi$ and $R_h = 1.4\xi$. Same notation as used in figure 2. The insets are phase plots in the equatorial plane illuminating the vortex states adjoin the change from $L = 3$ to $L = 7$, which correspond to points A and B in the energy curves.

Note however that all these competing interactions are fine-tuned by the size of the hole. As the size of the hole is increased, its influence on the vortex states grows. As a first result, we observed the 'necking' and even disappearance of some *symmetric* vortex states for larger holes in figure 5.

The proximity of the already trapped flux inside the hole to the equator of the sample hampers the entry of additional vortices. Instead, we found the surprising result that the suppression of superconductivity on the equatorial waist becomes energetically more favorable than the entrance of a single vortex. With increasing field however, the magnetic pressure for flux entry grows, and eventually overwhelms the repulsion by the trapped vortices. At that (large) field, a multi-vortex entry becomes possible, and we observe the simultaneous entry of several flux quanta. In the present case, we identified $R_h = 1.25\xi$ as a characteristic phase transition point, above which multi-quanta vortex entry is feasible. Note, e.g. the transition $L = 3 \rightarrow 7$ for $R_h = 1.40\xi$ (see figure 7), where the vortex states in between are *completely missing*, and even do not exist as metastable states. The entrance of these four vortices is a *continuous* process where near point A in figure 7, the four vortices nucleate at the equator of the sphere and move towards the central hole with increasing magnetic field. For $R_h = 1.50\xi$, the forces get in perfect balance, and *no vortex entry is possible beyond* $L = 4$, i.e. $n_o = L$ (instead, superconductivity is gradually destroyed from the waist inside). As n_o increases nonlinearly with further increase of R_h beyond 1.5ξ, our sample becomes effectively a narrow superconducting ring [2], and only trapped, giant-vortex states are found. This is illustrated in figure 8 for a sample with $R_h = 3.2\xi$, where free energy curves demonstrate approximately quantized stability of each vortex state.

To reinforce our message regarding the influence of hole-size on the flux patterns, we plot the Cooper-pair density of three vortex states in figure 9, all found for $L = 3$ but for different hole radii. For small R_h, one vortex is pinned and two remain on opposite sides of the hole; larger R_h attracts one more vortex, and a single remaining vortex resides on the sample periphery

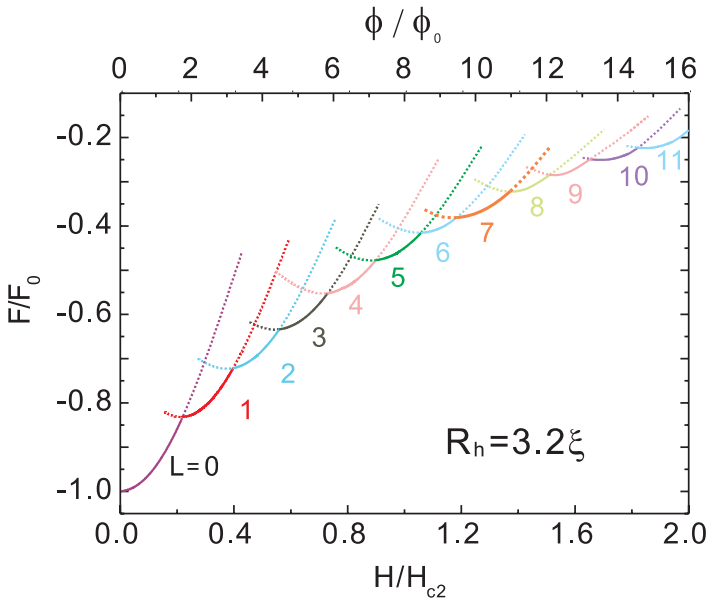

Figure 8. The free energy as a function of the applied magnetic field for a sphere of radius $R = 4\xi$, with a perforation of radius $R_h = 3.2\xi$.

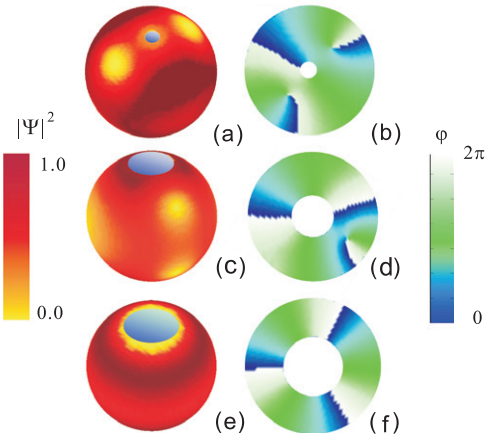

Figure 9. The surface plots of Cooper-pair density and the equatorial phase plots of $L = 3$ states in a $R = 4\xi$ sphere with a hole, i.e. $(n_o, L) = (1,3)$ state for $R_h = 0.4\xi$ and $H = 0.9H_{c2}$ (a) and (b); (2,3) state for $R_h = 1.2\xi$ and $H = 1.1H_{c2}$ (c) and (d), and (3,3) state for $R_h = 1.6\xi$ and $H = 1.3H_{c2}$ (e) and (f).

(broken-symmetry state); finally, for an even larger hole, all three vortices are trapped in the hole. Once more, we emphasize here that the broken symmetry states were found for vorticity up to $L = 3$, for hole radii for which $L - n_o = 1$, i.e. all vortices but one resided in the hole.

Due to its influence on the magnetic screening and intervortex interaction, the GL coefficient κ is clearly very important for the vortex states of broken symmetry. In figure 10, we show the calculated stability region of the asymmetric vortex configuration (1, 2) for values of the GL parameter κ between 0.8 and 2. We found that both lower and upper critical magnetic field for the stability of this state *decrease* with increasing κ, but their difference *increases*.

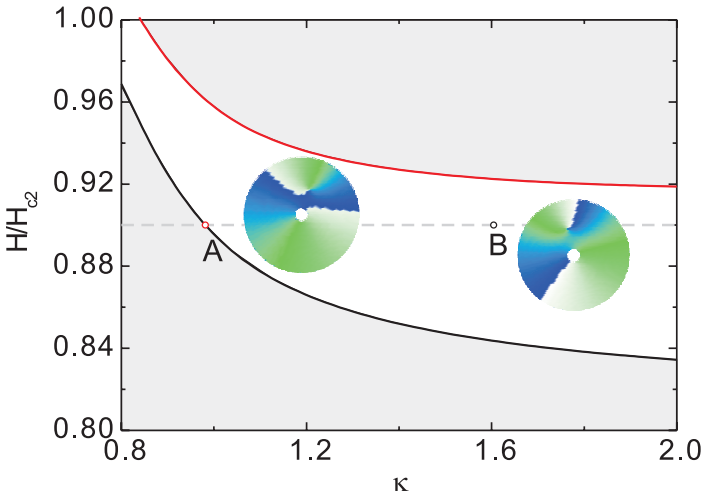

Figure 10. The field stability region (white area) of the asymmetric (1, 2) vortex state as function of the GL parameter κ. The phase plots in the equatorial plane are shown for applied magnetic field $H = 0.9H_{c2}$, and $\kappa = 0.9$ (point A) and $\kappa = 1.6$ (point B), to illustrate the varying distance between the hole and the strayed vortex.

This increasing of the field stability range becomes slower for samples with bigger κ especially when $\kappa > 2$. The two insets show the phase plots in the equatorial plane of the sample for two values of κ, 0.9 and 1.6. These illustrate that the single vortex gradually approaches the hole and the pinned vortex with decreasing κ. This is caused by the strengthened screening of the applied field towards the hole, and weakened inter-vortex repulsion, which both favor the formation of the giant vortex in the hole and leads to the narrowing of the stability range of the asymmetric vortex state.

The appearance of the broken symmetry states is characteristic for our spherical samples, which is absent in a superconducting cylinder. We briefly address here the properties of a cylinder with radius $R = 4\xi$ and thickness $d = 5.3\xi$, having the same volume as the sphere with radius $R = 4\xi$. After introducing the hole of radius $R_h = 0.4\xi$ in the cylinder, we repeated our study of the ground vortex states, and determined that states of broken symmetry are *not realizable* in this geometry (energy diagram and found states are shown in figure 11). Namely, the BL barrier in cylinders is much higher than in spheres, and vortices will enter the sample at higher fields, already strong enough to confine all vortices in the hole. Note also that all vortices entering the cylinder are straight, columnar objects, and BL barrier per length of the vortex is far higher then when the vortex enters in a single weak point on the equator of a sphere. In other words, the curvature of the sample surface appears to be essential for the stabilization of the broken symmetry state, almost as if the single vortex on the sample perimeter finds comfort in its 3D curving. As one reason, the self-energy of the vortex becomes significantly affected by its curved elongation and the consequent interaction between its top and bottom parts.

4. Sphere with central perforation in a tilted magnetic field

It is already known that thin, effectively 2D, superconductors bear weak sensitivity to an in-plane magnetic field, having the critical field in that direction scaling inversely to the sample

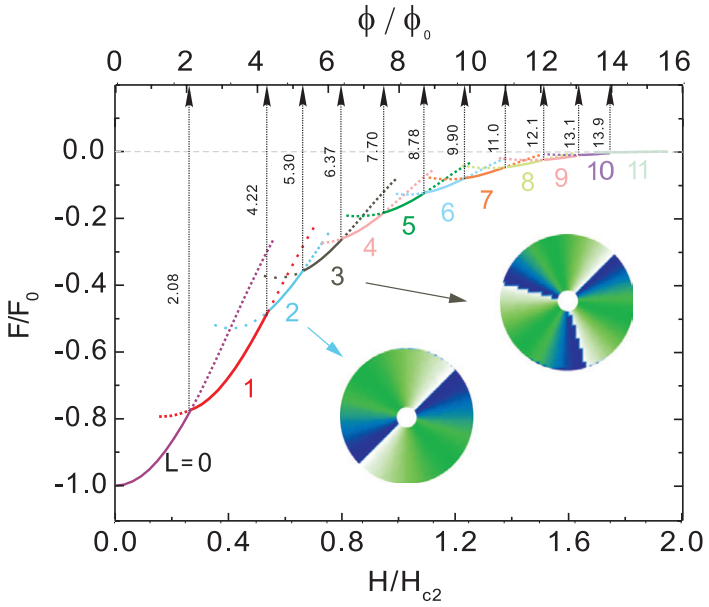

Figure 11. The free energy curves for a cylindrical superconductor with radius $R = 4\xi$, thickness $d = 5.3\xi$ and the radius of the central hole $R_h = 0.4\xi$. Insets show the contourplots of the superconducting phase for the vortex states $L = 2$ and $L = 3$.

thickness. In other words, the physics of vortex matter in such samples remains virtually unaffected by a tilted magnetic field, except for high-T_c superconductors where different spatial components of the field may lead to the appearance of crossing pancake and Josephson vortex lattices (see, e.g. [23]).

The tilt of the magnetic field with respect to peculiarities of the sample boundaries is obviously important for the vortex matter in 3D superconducting elements. There, 3D quantum confinement reflects through the interactions between the screening currents and the trapped flux lines, and consequently vortex phenomenology becomes far richer than in 2D cases. The behavior of mesoscopic cylinders and asymmetric spheres was recently studied in [15, 24] respectively, and unique giant-to-multi vortex splitting at the sample edge was found, and the influence of asymmetry-induced torque was discussed. In the present case, we analyze the influence of a cylindrical perforation on the superconducting properties of a mesoscopic sphere, with emphasis on the deterministic influence of the defect's geometry on the vortex states, and the interplay of competing symmetries, i.e. the one of the sample, the one of the introduced perforation, and the one stemming from the imposed direction of the applied field.

We continue the study using the same sample as in the preceding sections, i.e. a sphere with radius $R = 4.0\xi$, with a cylindrical perforation of radius $R_h = 1.2\xi$. The free energy curves and surface plots of the Cooper-pair density of vortex states in axially applied magnetic field ($\theta = 0^\circ$) were already shown in figure 4. In what follows, we gradually rotate the applied magnetic field from longitudinal ($\theta = 0^\circ$) to transverse direction ($\theta = 90^\circ$), with particular attention to $\theta = 30^\circ$, 45°, 60° and 90° cases.

Figure 12 shows the iso-surfaces of Cooper-pair density and the corresponding phase plots for vortex states with vorticity $L = 1 - 4$ ((a–d), respectively), found for $\theta = 30^\circ$. The

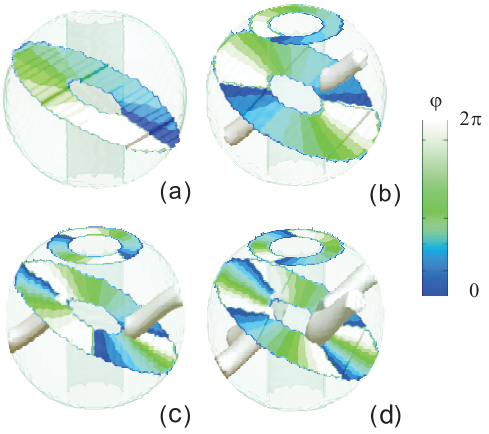

Figure 12. The phase of the order parameter in the plane perpendicular to the direction of the applied magnetic field (dark/white color—$0/2\pi$ phase) superimposed on the 10% 3D isoplot of the Cooper-pair density (smoothed) in the spherical sample with radius $R = 4\xi$ and circular perforation of radius $R_h = 1.2\xi$, in a magnetic field $H = 0.38H_{c2}$ (a), $H = 0.66H_{c2}$ (b), $H = 0.78H_{c2}$ (c), and $H = 1.06H_{c2}$ (d), tilted under angle $\theta = 30^\circ$ with respect to the perforation.

contourplots of the superconducting phase are given: (i) in the plane perpendicular to the applied magnetic field, indicating the total vorticity in the sample, and (ii) in the higher latitude plane, perpendicular to the perforation, showing the number of vortices trapped inside the hole. This emphasizes the point raised in [16], that the definition of vorticity in 3D is more complicated than in 2D, as the plane for needed contourplot of the phase is not uniquely defined.

As shown in figure 12(a), the single vortex case does not differ greatly from the $\theta = 0^\circ$ case, with a vortex being located inside the hole regardless of the tilt angle. We found such behavior of the $L = 1$ state up to a tilt angle of $\theta = 50^\circ$. The following flux line entering the sample in a $L = 2$ state finds its equilibrium position inside the superconductor, roughly aligning with the direction of the applied field (figure 12(b)). Note however that this vortex tube is interrupted by the hole, and remains perpendicular to the inner and outer surface of the sample in its both ends. Such discontinuity of the vortex line is particularly visible in figure 12(c), where third added vortex enters the hole due to competing interactions; due to strong interaction with doubly quantized vortex in the hole and associated screening currents, one remaining flux line in the sample is clearly disconnected in two equivalent parts, both equally shifted vertically from the symmetry axis with respect to the direction of the applied field. Note that very similar behavior of a single vortex can be obtained in two completely separated semi-spheres. However, further increase of vorticity restores the full influence of the sample geometry. For $L = 4$, two flux lines in the superconducting part of the sample in figure 12(d) show similar behavior to the one of figure 12(c), but also minimize their energy by arranging along the parallels of latitude of the sample.

In figure 13, free energy curves are plotted as a function of the magnitude of the applied magnetic field for the above discussed sample. Compared to the free energy curves in the $\theta = 0^\circ$ case (see figure 4), all the less energetically favorable vortex states (e.g. $L = 4$ and $L = 5$), become more stable for $\theta = 30^\circ$. Namely, their unique properties discussed in section 3 were a

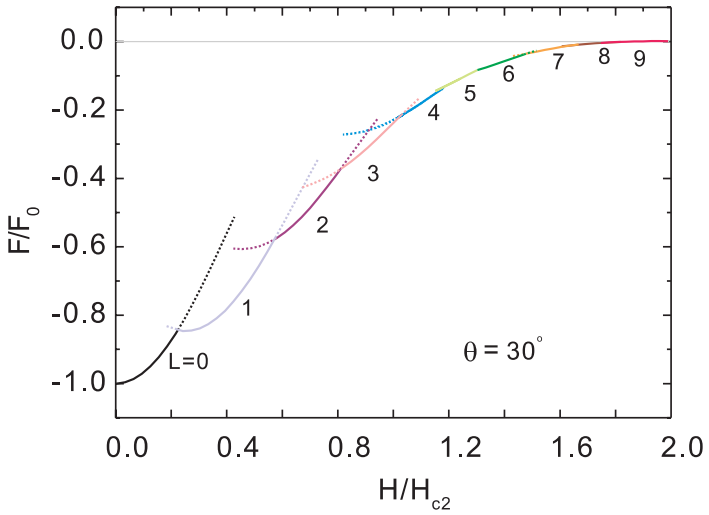

Figure 13. The free energy curves as a function of the applied magnetic field, for a superconducting sample with radius $R = 4.0\xi$ and $R_h = 1.2\xi$, the magnetic field is applied in a tilt angle $\theta = 30^\circ$.

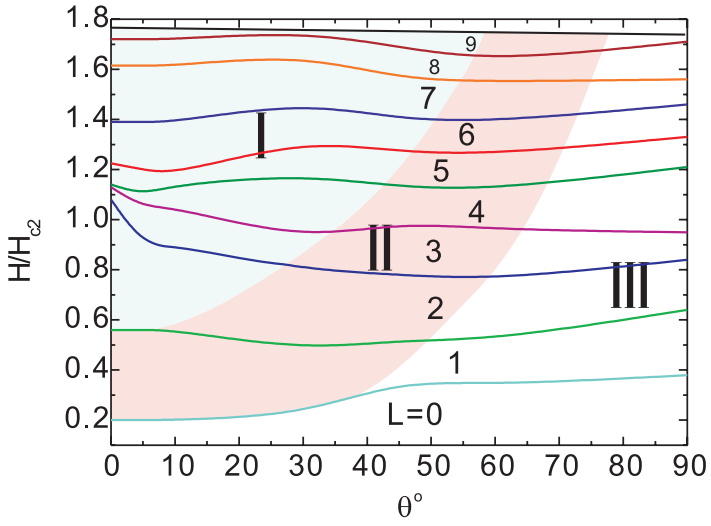

Figure 14. The same samples as figure 13, the stability regions for different vortex states are plotted as function of the angle θ of tilting magnetic field. Areas I, II and III index vortex configuration with different numbers of vortices inside the hole, which equal 2, 1 and 0 respectively (shown in different colors).

direct consequence of the interaction with the perforation, whose influence ceases with increase of the tilt angle θ. For example, the stability range of the $L = 1$ and $L = 2$ state gradually decreases when the tilt angle θ is increased to 60°, while at the same time those ranges for $L = 3$, 4 and 5 increase (see figure 14). Namely, the increased deviation of the angle from the direction of the perforation *decreases* the stray flux through the hole and enhances the screening effects. As a consequence, the stability range of the Meissner state broadens in the ground-state, at the expense of the $L = 1$ state.

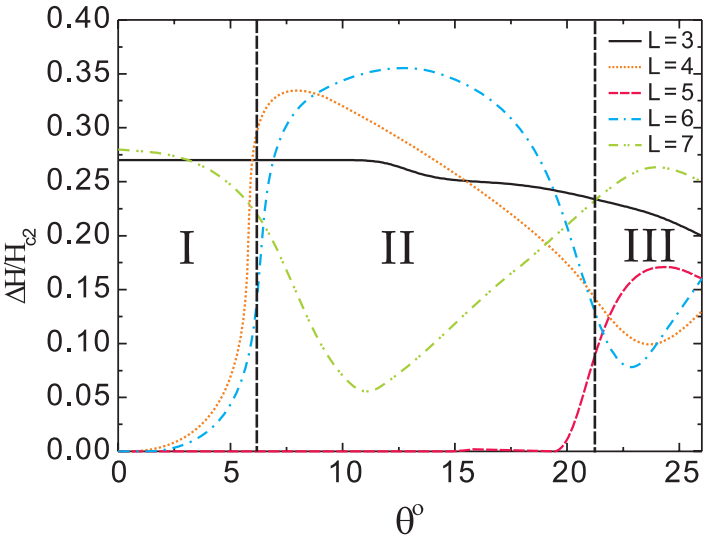

Figure 15. The stability regions ΔH for vortex states 3, 4, 5, 6 and 7, versus the tilting angle θ of the applied magnetic field, for sample with radius $R = 4\xi$ and circular perforation of radius $R_h = 1.4\xi$. The region I, II and III index the areas where $n_c = 0$, 1 and 2, respectively.

The number of vortices trapped inside the hole increases with the tilting of the magnetic field, which plays an important role in the behavior of the vortex entrance. To get a complete understanding of this phenomenon, we carried out the calculation by scanning the field up/down for a series of fields for different tilt angle θ. Here, one more parameter n_c is introduced to indicate the number of vortices that cross the hole with both ends extend along the field direction. Indeed, we found that in the case of $n_s = 3$, the n_c increased from 0 to 1 (with total vorticity equals 4, when θ increased from 0° to 6°), and then to 2, where total vorticity equals 5 ($\theta = 22°$). And its' influence on the entrance behavior can be concluded from figure 15, where the stability region ΔH for the different vortices are plotted as function of the tilting angle of the field, for the sample with radius $R = 4\xi$ and circular perforation of radius $R_h = 1.4\xi$. Apparently, the aforementioned $3 \rightarrow 7$ transition is shown in region I, for $\theta = 0° \rightarrow 6°$. When $\theta > 6°$, the $L > 4$ and the multivortex entrance is now $L = 4 \rightarrow 6$ (see figure 15). Whereas the $L = 7$ vortex state is compressed by the waist inwards due to the penetration of the magnetic field, especially for the cases with larger stability of $L = 4$ and 6. The compression becomes weaker when the field is tilted markedly, where the $L = 4$ and 6 is not as dominant as in the smaller angle cases. This interaction of the stability between border vortex states continuous until $\theta = 22°$, where the $L = 5$ with $n_c = 2$ can be the ground state, and at the same time the continuous penetration of a single vortex becomes possible resulting in transitions like $3 \rightarrow 4 \rightarrow 5 \rightarrow 6 \rightarrow 7$ as found earlier for a full sphere [16].

With the increase of the tilt angle (figure 14), the magnetic field becomes more dominant in directing the nucleating vortices, i.e. vortex lines lie preferentially in the direction of the field. This is illustrated in figure 16, where the iso-surfaces of Cooper-pair density and the phase plots are shown for the $\theta = 60°$ case. The first obvious difference in comparison with figure 12 is that the hole becomes less able to trap vortices for larger tilt angles. As a consequence, the $L = 3$ state in figure 16(c) now resembles the $L = 4$ state in figure 12(d), while the present

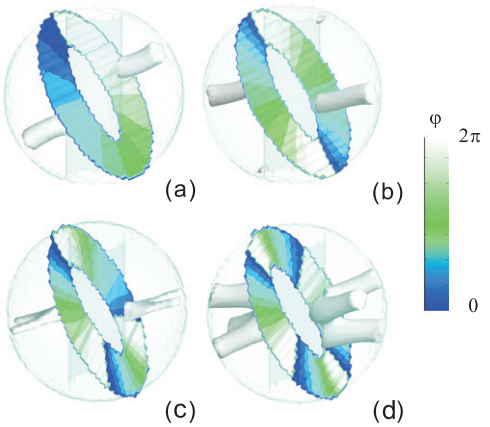

Figure 16. Same as figure 12, but now for a tilt angle $\theta = 60^\circ$ and magnitude of the field $H = 0.44H_{c2}$ (a), $H = 0.66H_{c2}$ (b), $H = 0.97H_{c2}$ (c) and $H = 1.01H_{c2}$ (d).

$L = 4$ configuration shows three entwining vortex lines outside the hole. It is easy to conclude that final vortex arrangement strongly depends on the number of flux quanta inside the hole, as this influences both the vortex–vortex interaction in the system as well as the intensity of the screening currents around the hole and along the perimeter (in 3D). In figure 14, the number of vortices inside the perforation is shown for different total vorticity inside the sample. For the chosen geometric parameters of the sample, maximum two vortices may be confined inside the hole for $L > 2$ and $\theta = 30^\circ$ and for $L > 4$ and $\theta = 45^\circ$. This shows that hole occupation number depends on the overall interactions in the system, i.e. not only size of the hole and tilt angle of the field, but also the number of present flux lines which tend to reduce their density and minimize their mutual repulsion by pushing some of the vortices inside the hole. Still, no more than one vortex was found residing in the hole, regardless of total vorticity, for $\theta > 57^\circ$, and no vortices at all were found in the hole for angles $\theta > 83^\circ$.

The fact that some of the vortex lines for a given tilted applied field stray into the hole is not only important for the final vortex configuration, but it also has certain experimental consequences. Namely, one of the regularly used experimental methods for studies of flux behavior in superconductors is Hall magnetometry, where a Hall probe placed above (or below) the sample, in the direction of applied field, is used to detect the magnetic response of the sample [25] (see inset of figure 17(a)). The typical magnetic signal of a mesoscopic superconductor would comprise quantized jumps in the magnetization in increased magnetic field, each associated with a vortex entry (carrying roughly a flux quantum) [26]. Using equation (5), we calculated the magnetization of our oblate samples in the direction of the applied field, through an imaginary Hall probe much larger than the sample itself, placed at distance ξ above the sample. Results are shown in figure 17(a), for tilt angle of the field $\theta = 60^\circ$. It is immediately apparent that not all found jumps in magnetization curves in a sweep-up regime are of equal size, as some of them appear to be carrying fractional flux [27]. However, situation becomes inverted in figure 17(b), where the Hall probe was placed above the hole, not in the direction of the field. Therefore, the three-dimensionality of the structure plays a trick on the magnetic measurement, as vortices guided away from the probe by the perforation in figure 17(a), manifest on the magnetization curve as an effectively fractional jump, with relative

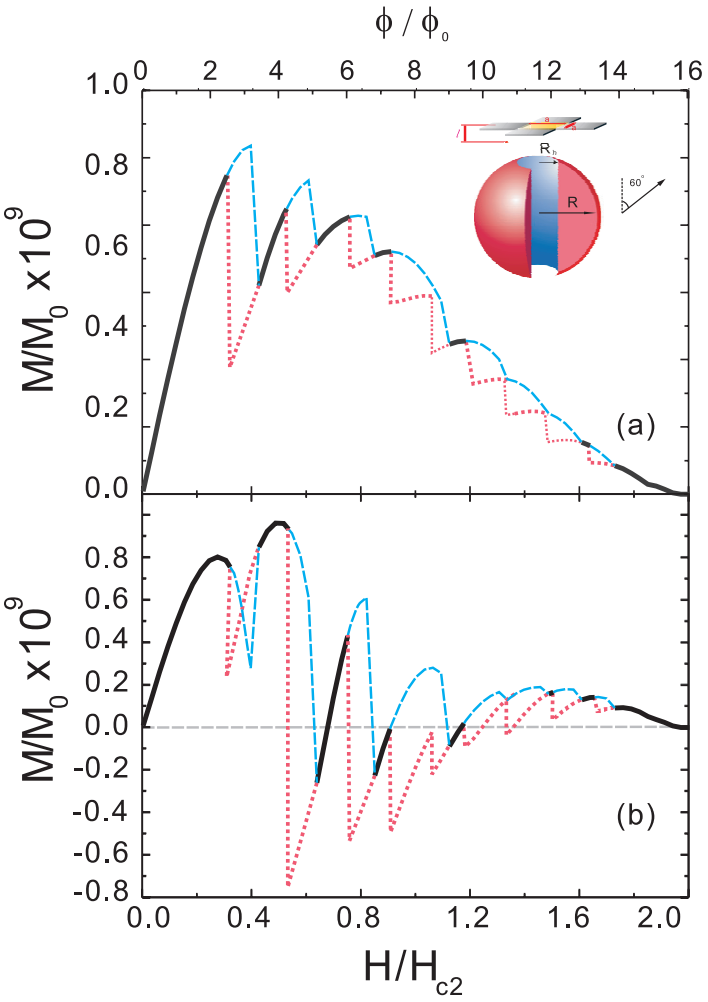

Figure 17. Magnetization as function of the applied magnetic field H, as obtained from a Hall magnetometer (with size $a > 2R$) placed in the direction of applied field (a), or above the perforation (b), in the case where magnetic field is directed $\theta = 60^\circ$ from the cylindrical hole. The dashed lines indicate the process of magnetic field sweeping up, dotted lines for sweeping down and solid lines for regions which exist in both processes.

size of $2.8\Phi_0$ for $\theta = 60^\circ$ compared to the full Φ_0 jumps. Note also that channeled flux decays with increasing field for vortices present in the sample.

In the above discussion, we have deliberately neglected the $\theta = 90^\circ$ case; this case is naturally similar to the above ones as it follows the others by gradual increase of the tilt angle of the applied field. However, with field being completely perpendicular to the perforation (the applied field practically does not 'see' the perforation), and with no vortices being trapped by the hole (see figure 14), this case requires special attention. The isoplots of obtained vortex configurations are shown in figure 18. In our study of the different tilt angles for the applied field, vortices were always attracted by the hole, being ultimately completely trapped inside of it, or just piercing through the cylindrical perforation. Note however that in the latter case vortex lines always formed polygonal structures on the sample surface, due to their mutual repulsion.

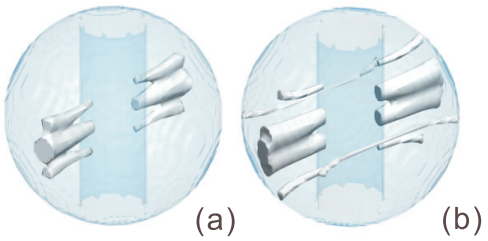

Figure 18. The 10% 3D isoplots of the Cooper-pair density in the sample in transversely applied magnetic field $\theta = 90^\circ$, for (a) fields $H = 0.97H_{c2}$ and (b) $H = 1.31H_{c2}$.

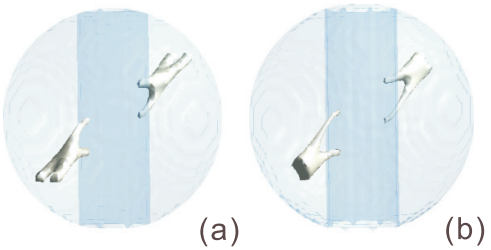

Figure 19. The 30% 3D isoplots of the Cooper-pair density, illustrating the unique structural vortex transition in a sphere with radius $R = 4\xi$ and perforation of $R_h = 1.2\xi$, at magnetic field $H = 0.85H_{c2}$ (a) and $H = 1.06H_{c2}$ (b) applied under angle $\theta = 45^\circ$, both for vortex state $L = 3$.

In the present case, the pinning of vortices by the perforation results in 1D vortex matter, as flux lines arrange along the hole in a linear fashion. The maximal number of vortices along a single line is $L = 5$, and subsequent vortices at higher fields pierce the sample side of the hole, preserving the mirror symmetry of the vortex state (see figure 18(b)). This vortex ordering is obviously influence by the size of the sample and the radius of the perforation, as flux lines see the perforation as a strip of width $2R_h$. Therefore, rich structural transitions between linear and zig-zag pinned vortex patterns can be expected in this system [28], bearing in mind the interaction of those same vortices on the curved surface of the sample.

Vortex chains observed in the $\theta = 90^\circ$ case, and vortex states consisting of pinned (trapped in the hole) and tilted flux lines in other cases are characteristic vortex configurations for the unique sample geometry in this study. However, besides the sample geometry and tilt angle of the applied field, the actual value of the applied magnetic field is a very important factor for the vortex matter in this system. For one thing, it determines the number of vortices in the sample whose inter-vortex repulsion is one of the key elements in the formation of the vortex state. However, the exact value of the applied field also induces the corresponding screening response of the sample, i.e. for a fixed vorticity, slow changes of the applied field result in varying intensity of the Meissner currents across the sample. This again affects the vortex lines, increasing/decreasing the magnetic pressure exerted on them towards particular parts of the sample. Typical vortex re-configurations due to this effect are shown in figures 19 and 20.

We have identified earlier the number of vortices trapped inside the hole as one of the prominent features of vortex matter in perforated spheres. Figure 20 shows the fine influence of gradually changing applied magnetic field on the latter key property. Namely, we have shown

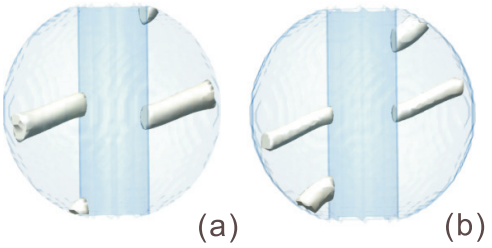

Figure 20. Same as in figure 19, but for a tilt angle $\theta = 60^\circ$, with (a) $H = 0.55H_{c2}$ and (b) $H = 0.72H_{c2}$.

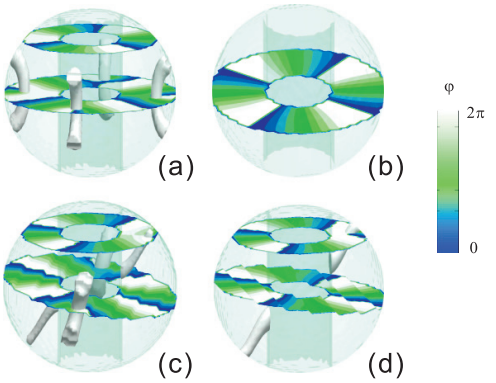

Figure 21. The phase of the order parameter in the plane perpendicular to the direction of the applied magnetic field (dark/white color—$0/2\pi$ phase) superimposed on the 10% 3D isoplot of the Cooper-pair density in the spherical sample with radius $R = 4\xi$ and circular perforation of radius $R_h = 1.4\xi$, in a magnetic field $H = 1.43H_{c2}$ (a), $H = 1.45H_{c2}$ (b), $H = 1.39H_{c2}$ (c), and $H = 1.36H_{c2}$ (d), the tilting angle is $\theta = 1^\circ$ for upper layer, and $\theta = 10^\circ$ for lower layer, with $n_c = 1$.

that in the $\theta = 0^\circ$ case vortices become more compressed towards the hole when magnetic field is increased. However, in the $\theta > 0^\circ$ case this is quite opposite as the trapped flux line as well as the magnetic flux inside the hole may gradually emerge from it when the magnitude of the applied field is raised. Figure 20 shows a sequence of images of this unique vortex deconfinement transition, obtained for the $L = 2$ state in the $\theta = 60^\circ$ case.

Differently from the vortex state shown in figure 16(c) where two individual vortices on the surface coalesced into a perforation, figure 20(a) shows the state with two anti-crossing vortices. In desire to remain orthogonal to the inner surface of the sample (i.e. cylindrical hole), two vortices are arranged one above the other, while remaining next to each other on the outer surface of the sample. However, with increasing magnetic field, the balance of all forces in the system causes rearrangement of the flux lines, removes the energy costly crossing and reduces the length of each vortex line. As a result, vortices are finally parallel to each other, in the plane defined by the meridian of the sample and the sample axis (figure 20(b)).

It is interesting to study how the multi-vortex entry phenomenon found in the previous section is influenced by tilting the magnetic field. There, we found the remarkable *continuous*

transition $L = 3 \rightarrow 7$ when the field increases, as a process of the nucleation of four vortices at the equator of the sphere. When the applied magnetic field is tilted slightly away from the z-axis from 1° to 5°, we observed the *reduced* stability region of this continuous process of vorticity change, from $\Delta H = 0.061 H_{c2}$ for angle $\theta = 1^\circ$ to $\Delta H = 0.03 H_{c2}$ for $\theta = 5^\circ$. The vortex state (3,7) is always found to be the ground state in these cases, while at the same time, the metastable state (4,4) is found. Both vortex states are shown in figures 21(a) and (b). The energy difference between these two states decreases with tilting of the field. For example, one of the four hole-bound vortices for the (4,4) state extends outside of the hole (see figure 21(d)), following the field direction, which lowers the energy of the whole system. Even for the (3,7) state, two vortices on the side of the hole can also penetrate deeper inside the sample because of the weaker repulsion from the central current around the hole. As a result of this, the other two vortices are generally pushed away from the hole. These two vortex states (3,7) and (4,4) become energetically comparable when the tilting angle becomes larger than 6°, where (4,4) is stable, and (4,6) can be found for higher magnetic field.

5. Conclusions

In this work, the superconducting properties and vortex behavior are thoroughly studied in a mesoscopic superconducting sphere with a cylindrical perforation. Full three-dimensionality of demagnetization effects is taken into account, in a self-consistent numerical solution of the GL equations. We reported different vortex configurations, defined by the interplay of competing symmetries in the system, by changing the size of the perforation, direction of the applied field and GL parameter κ. For applied field parallel to the hole, we discovered unique asymmetric vortex ordering, never found in the case of superconducting cylinders, stemming from the competition of the symmetry of the perforation and the sample outline.

We constructed a R_h–H vortex phase diagram, where the appearance of asymmetric states in the ground state, as well as of multi-vortex states and multi-quanta vortices pinned by the hole are discussed as a function of the hole size (R_h) and applied field (H). We also found a series of non-uniform transitions in vorticity versus applied field for intermediate sizes of the hole, in a specific regime in which our sample has little resemblance in behavior to either the full sphere, or thin ring limit.

In the case when the applied field was tilted with respect to the sample axis, we analyzed the competing interactions in the system that guide the flux lines in the sample either along the direction of the field, or completely inside the perforation. For different tilt angles θ, we studied the vortex configurations, the transitions between them, and the number of flux quanta trapped in the hole. Analyzed transitions include ones for fixed vorticity, where we found novel vortex reordering and vortex deconfinement from the hole as a function of slowly varying field. We also studied the magnetic response of vortex states when a Hall probe was placed in the direction of applied field, or above the perforation; due to the three-dimensionality of the vortex structure, we identified features on the $M(H)$ curves that correspond to vortex entry, but appear to carry fractional flux when measured by Hall magnetometry. Moreover, the magnetic signal contains features related to each vortex entry, effectively seeing the perforation as a pinning channel while simultaneously arranging on the curved outer surface of the sample.

Surprisingly, multivortex entry was found in our calculation for samples with certain sized holes. Here the originally first-order phase transition between different vortex states appears to be a semi-first order one. By tilting the applied magnetic field, we are able to understand the

complicated 3D interactions between vortices and the boundary of the samples, which are the reasons for this particular phenomenon.

Acknowledgments

This work was supported by the Flemish Science Foundation (FWO-Vl), the Interuniversity Attraction Poles (IAP) Program—Belgian State—Belgian Science Policy, ESF-JSPS NES program and the ESF-AQDJJ network. MVM acknowledges support from the EU Marie Curie Intra-European program.

References

[1] Tinkham M 1996 *Introduction to Superconductivity* (New York: McGraw-Hill)
[2] Baelus B J, Peeters F M and Schweigert V A 2000 *Phys. Rev.* B **61** 9734
[3] Vodolazov D Y, Baelus B J and Peeters F M 2002 *Phys. Rev.* B **66** 054531
[4] Kanda A, Baelus B J, Vodolazov D Y, Berger J, Furugen R, Ootuka Y and Peeters F M 2007 *Phys. Rev.* B **76** 094519
[5] Misko V R, Savel'ev S and Nori F 2006 *Phys. Rev.* B **74** 024522
[6] Silhanek A V, Van Look L, Raedts S, Jonckheere R and Moshchalkov V V 2003 *Phys. Rev.* B **68** 214504
[7] Silhanek A V, Van Look L, Jonckheere R, Zhu B Y, Raedts S and Moshchalkov V V 2005 *Phys. Rev.* B **72** 014507
[8] Berdiyorov G R, Milošević M V and Peeters F M 2006 *Phys. Rev. Lett.* **96** 207001
[9] Berdiyorov G R, Milošević M V, Baelus B J and Peeters F M 2004 *Phys. Rev.* B **70** 024508
[10] Xiao Z-L, Han C Y, Kwok W-K, Wang H H, Welp U, Wang J and Crabtree G W 2004 *J. Am. Chem. Soc.* **126** 2316
[11] Qiang Du 2005 *J. Math. Phys.* **46** 095109
[12] Gladilin V N, Tempere J, Silvera I F, Devreese J T and Moshchalkov V V 2008 *Phys. Rev.* B **77** 024512
[13] Baelus B J, Sun D and Peeters F M 2007 *Phys. Rev.* B **75** 174523
[14] Doria M M, de C Romaguera A R and Peeters F M 2007 *Phys. Rev.* B **75** 064505
[15] de C Romaguera A R, Doria M M and Peeters F M 2007 *Phys. Rev.* B **75** 184525
[16] Xu B, Milošević M V and Peeters F M 2008 *Phys. Rev.* B **77** 144509
[17] Doria M M and Zebende G F 2002 *Phys. Rev.* B **66** 064519
[18] Enomoto Y, Kato R and Maekawa S 1993 *Phys. Rev.* B **47** 8016
[19] Schweigert V A and Peeters F M 1998 *Phys. Rev.* B **57** 13817
[20] Mkrtchyan G S and Shmidt V V 1972 *Sov. Phys.—JETP* **34** 195
[21] Berdiyorov G R, Milošević M V and Peeters F M 2006 *Phys. Rev.* B **74** 174512
[22] Milošević M V, Rakib M T I and Peeters F M 2007 *Europhys. Lett.* **77** 27005
[23] Grigorenko A N, Bending S J, Grigorieva I V, Koshelev A E, Tamegai T and Ooi S 2005 *Phys. Rev. Lett.* **94** 067001
[24] de C Romaguera A R, Doria M M and Peeters F M 2007 *Phys. Rev.* B **76** 020505
[25] Oral A, Bending S J and Henini M 1996 *Appl. Phys. Lett.* **69** 1324
[26] Geim A K, Grigorieva I V, Dubonos S V, Lok J G S, Maan J C, Filippov A E and Peeters F M 1997 *Nature* **390** 259
[27] Geim A K, Dubonos S V, Grigorieva I V, Novoselov K S, Peeters F M and Schweigert V A 2000 *Nature* **407** 55
[28] Piacente G, Schweigert I V, Betouras J J and Peeters F M 2004 *Phys. Rev.* B **69** 045324